

RESEARCH ARTICLE

Mechanism of Ammonia Oxidation to Dinitrogen, Nitrite, and Nitrate on β -Ni(OH)₂ from First-Principles Simulations

Dr. Rachelle M. Choueiri¹ | Stephen W. Tatarchuk² | Prof. Anna Klinkova² | Prof. Leanne D. Chen^{*1}

¹Electrochemical Technology Centre,
Department of Chemistry, University of
Guelph, Ontario, Canada

²Department of Chemistry and Waterloo
Institute for Nanotechnology, University of
Waterloo, Ontario, Canada

Correspondence

Prof. Leanne D. Chen, Electrochemical
Technology Centre, Department of
Chemistry, University of Guelph, 50 Stone
Road East, Guelph, Ontario N1G 2W1,
Canada
Email: leanne.chen@uoguelph.ca

Abstract

The electrocatalyzed ammonia oxidation reaction (AOR) is a potential pathway toward waste ammonia remediation, energy generation, and the synthesis of value-added products. To date, mechanistic studies have focused on elucidating the progress of AOR on Pt-based catalysts with an established pathway for N₂ only. In this work, density functional theory was applied to determine the lowest energy intermediates towards nitrogen gas, nitrite, and nitrate formation on β -Ni(OH)₂, a promising electrocatalyst material for AOR. It was found that dinitrogen formation progresses via NH-NH coupling while nitrite and nitrate formation occurs via deprotonation to adsorbed N and subsequent hydroxylation to form oxygenated intermediates. This work is the first to report a mechanism for nitrite and nitrate formation and will also serve as a benchmark for future studies on Ni-based materials.

KEYWORDS:

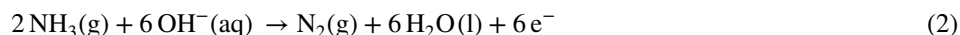
ammonia oxidation reaction, density functional theory, electrocatalysis, nickel hydroxide

1 | INTRODUCTION

The electrochemical ammonia oxidation reaction (AOR) is a promising method for the conversion of ammonia into energy or value-added products.^{1,2,3} It is also a potential alternative to current waste ammonia remediation practices as it does not form noxious by-products such as NO_x gases and can be accomplished at ambient conditions.⁴ Another advantage is the low theoretical overpotential required for AOR, for which the thermodynamic equilibrium potential U° is only 0.0567 V vs. the reversible hydrogen electrode (RHE) for N₂ production. AOR has also been explored as an alternative anodic reaction to the oxygen evolution reaction (OER) for paired electrolysis with carbon dioxide reduction reactions, as OER requires a much larger energy input ($U^\circ = 1.23 \text{ V}_{\text{RHE}}$).⁵ On its own, the AOR is normally written as an oxidation reaction, in acid (pH = 0):

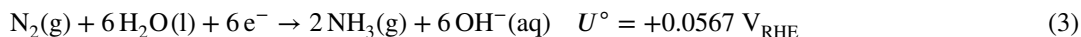


and in base (pH = 14):

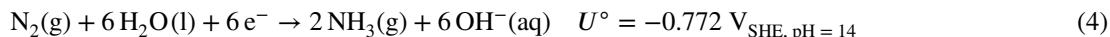


⁰**Abbreviations:** AOR, ammonia oxidation reaction; ASE, atomic simulation environment; BEEF-vdW, Bayesian error estimation functional with van der Waals correlation; CHE, computational hydrogen electrode; DFT, density functional theory; FED, free energy diagram; NRR, nitrogen reduction reaction; OER, oxygen evolution reaction; PAW, projector augmented wave; RHE, reversible hydrogen electrode; SHE, standard hydrogen electrode; UOR, urea oxidation reaction; VASP, Vienna ab initio simulation package.

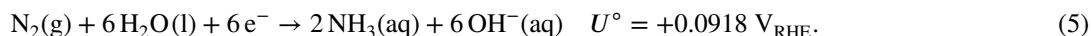
where the pH conditions are enforced by the presence of H^+ and OH^- respectively, as the standard state of all aqueous species is 1 M. Hereafter we will write this reaction with OH^- , since AOR experiments are carried out in alkaline conditions. It is paramount to note that care must be taken in placing this reaction based on its potential in the electrochemical series, in which redox reactions are always written as reductions. Therefore, we will strictly follow this convention in this work to avoid any ambiguity over the spontaneity of the reaction, and write the AOR in its reverse form: the nitrogen reduction reaction (NRR).



The standard reduction potentials of reactions involving an equal number of proton/hydroxide and electron transfers (including AOR/NRR as shown above) are invariant on the RHE scale, because the RHE itself varies with pH with the same slope. On the standard hydrogen electrode (SHE) scale, the standard reduction potential takes on a different value (at pH 14):



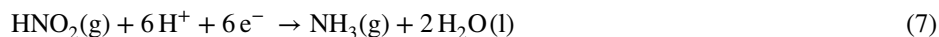
To be clear, the reduction of dinitrogen to ammonia is spontaneous with a negative standard Gibbs free energy of reaction $\Delta_r G^\circ$, while the oxidation of ammonia to dinitrogen is non-spontaneous with a positive $\Delta_r G^\circ$. These values are calculated from the standard Gibbs free energies of formation $\Delta_f G^\circ$ of all species involved in the reaction; a detailed calculation is shown in the Supporting Information (SI). We would also like to point out that a slightly different value may be obtained by using $NH_3(aq)$ instead of $NH_3(g)$ as the reference state, for which the standard reduction potential is



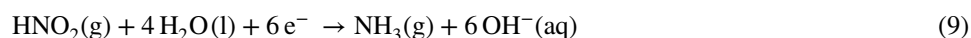
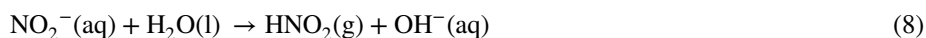
For AOR occurring at ambient temperature and pressure in electrolytic cells, basic anolytes ranging from pH 9–14 are employed to facilitate the successive deprotonation of *NH_x species (we will be using the asterisk symbol to denote an adsorbed species). The two dominant mechanisms of AOR towards nitrogen gas formation are the Oswin-Salomon mechanism,⁶ where *NH_x species are successively oxidized to form two *N which undergo coupling to form N_2 gas, and the Gerischer-Mauerer mechanism,⁷ a pathway where NH_3 is deprotonated into various *NH_x species that couple to form $^*NH_x-NH_y$ before further deprotonation to dinitrogen.

While AOR has been observed on various metals, the majority of mechanistic studies^{8,9,10,11,12,13,14,15,16,17} have been conducted on Pt-based catalysts due to their high activity owing to platinum's ability to facilitate the initial *NH_x deprotonation steps.^{18,19} AOR on Pt primarily occurs on the (100) facet,²⁰ forms $N_2(g)$ as a major product,²¹ and proceeds at low overpotentials compared to many other AOR-active metals.¹⁸ On the (100) facet, the Gerischer-Mauerer mechanism has been demonstrated to be the most thermodynamically favourable, with $^*NH-NH$ as the favoured coupling intermediate.¹² However, while nitrogen gas formation is initially facile, Pt-based catalysts suffer from short lifetimes and deteriorating currents due to poisoning. Depending on the potential range applied during electrolysis, Pt may be poisoned by *N or oxygenated species such as *NO .^{16,22} While further experimental work has been devoted to improving Pt performance via binary and ternary alloying, there is also considerable interest in developing electrocatalysts based on less expensive metals, which can potentially overcome these shortfalls.

Calculating the standard reduction potentials for nitrite and nitrate is somewhat more involved, as the number of protons/hydroxides and electrons transferred are not equal, implying a non-standard slope on the Pourbaix diagram. We will then make two separate calculations, one at pH 0, and another at pH 14, both referenced to the SHE because it makes more sense to work with an absolute rather than relative reference in this case. We begin by splitting each equation into two steps. For nitrite, these are



at pH 0 and



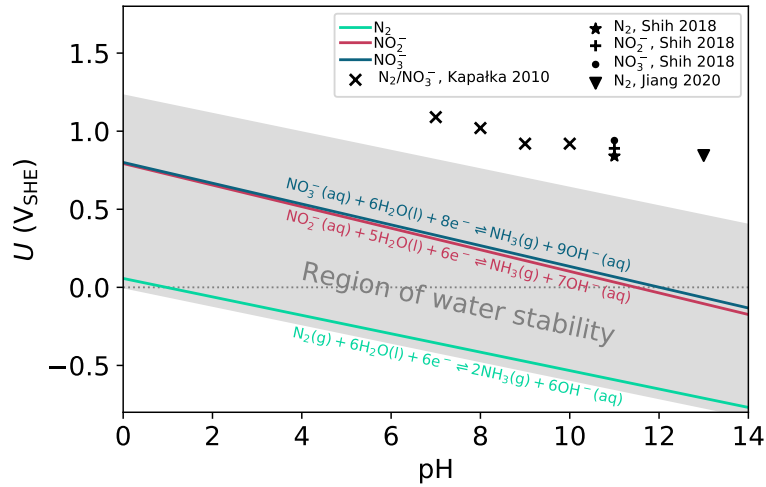
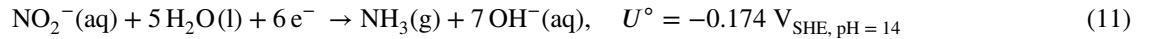


FIGURE 1 (a) Pourbaix diagram with thermodynamic equilibrium potentials and experimental onset potentials for AOR towards $\text{N}_2(\text{g})$, $\text{NO}_2^-(\text{aq})$, and $\text{NO}_3^-(\text{aq})$. Experimental onset potentials are converted to U_{SHE} from the corresponding experimental references.^{27,29,30}

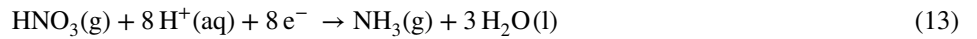
at pH 14. The standard Gibbs free energies of reaction $\Delta_r G^\ominus$ are calculated for each equation,²³ and summed for each pair under different pH conditions to yield standard Gibbs free energies of reaction $\Delta_r G^\ominus$. These standard Gibbs free energies of reaction are then divided by the number of electrons (and -1) to obtain the standard reduction potential for the overall process of nitrite reduction to ammonia (for calculation details, see the SI).



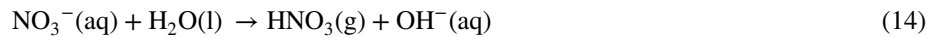
and



A very similar set of calculations are carried out for nitrate, beginning with writing the process in two parts in both acid



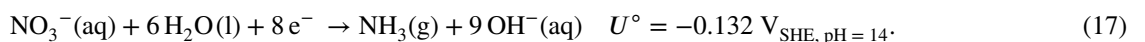
and base



Again we calculate the Gibbs free energies of reaction $\Delta_r G^\ominus$ using tabulated Gibbs free energies of formation $\Delta_f G^\ominus$ for the individual species²³ and obtain the following standard reduction potentials for nitrate reduction to ammonia:



and



To summarize these standard reduction potentials, Figure 1 shows the Pourbaix diagram of AOR to dinitrogen, nitrite, and nitrate formation. The solid lines represent standard reduction potentials that were summarized in the preceding paragraphs and calculated from thermodynamic literature data,²³ while the points represent values from experimental work on β -Ni(OH)₂/NiOOH. The lines for nitrite and nitrate reduction have non-standard, different slopes, and nearly cross at low pH values. It is worth noting that the differences between thermodynamic equilibrium potentials and experimental onset ones are quite large for all three reactions, indicating much room for catalyst improvement to approach the thermodynamic values and increase the energy efficiency of these processes.

Recent experimental work studying AOR on β -Ni(OH)₂/NiOOH-based catalysts, a system that has been studied in the context of the OER²⁴ and the urea oxidation reaction (UOR),^{25,26} has demonstrated significant improvements in catalyst lifetime and current for both pure and multi-metal β -Ni(OH)₂/NiOOH-based catalysts.^{27,28,29,30} In these studies, while N₂ gas is a major product, nitrite and nitrate anions are also produced in significant quantities depending on the applied potential and catalyst composition. At low overpotentials on pure β -Ni(OH)₂/NiOOH, dinitrogen is the major AOR product. With increasing potential, the formation of nitrite and nitrate species then becomes significant. These observations differ from studies on Pt, which only produces nitrite and nitrate in small amounts at high overpotentials. Consequently, NO₂⁻ and NO₃⁻ are only produced with concomitant oxidation of the Pt surface, in addition to the formation of other gaseous species such as N₂O.²²

Despite advantages of cost and catalyst lifetime, β -Ni(OH)₂/NiOOH-based catalysts suffer from high onset potentials above 1 V vs. the standard hydrogen electrode (SHE), even for dinitrogen production. Furthermore, the mechanism of AOR on these surfaces is still under development, and the identities of limiting steps and potential poisons are under debate. Thus, it is the aim of this work to formulate a mechanism for AOR on β -Ni(OH)₂ toward N₂, NO₂⁻, and NO₃⁻ using density functional theory (DFT) calculations as a first step towards understanding the unique characteristics of Ni(OH)₂-based catalysts in the context of these reactions. It should be noted that the catalysts used in the experimental AOR literature are prepared from β -Ni(OH)₂ by charging the hydroxide surface with a series of potential scans to produce a mixture of β -Ni(OH)₂ and β -NiOOH;³¹ for the present study we focus only on β -Ni(OH)₂ as it is a more idealized representation of the catalyst surface and will serve as a baseline for the electrocatalytic activity. By modelling the free energy of various possible intermediates on the nickel hydroxide surface, we set out to narrow down the most likely pathways and identify potential reaction bottlenecks which we will describe in what follows.

2 | COMPUTATIONAL DETAILS

All DFT calculations are performed with the Vienna Ab initio Simulation Package (VASP, version 5.4.4)^{32,33,34} using the Atomic Simulation Environment (ASE) interface.³⁵ Electronic interactions are described with the BEEF-vdW exchange-correlation functional³⁶, and the core electrons with pseudopotentials derived from the Projector Augmented Wave (PAW) approach supplied with VASP.^{37,38} Spin-polarized calculations are carried out with Ni magnetic moments initialized in the antiferromagnetic configuration in the *z* direction with $S_z = \pm 1.8\mu_B$, close to an experimentally determined value of $2.0 \pm 0.2\mu_B$.³⁹ The generalized gradient approximation with Hubbard *U* correction potential (GGA + *U*) is used to account for repulsive interactions of Ni *d*-electrons.^{40,41} The value of $U - J$ is 5.5 eV in our study, which was determined in a prior work that matched β -Ni(OH)₂ bandgap computed with BEEF-vdW + *U* to experiment using this Hubbard *U* value.^{26,42}

As the starting point for our DFT calculations, the experimentally determined β -Ni(OH)₂ bulk structure (mp-27912)^{39,43} was obtained from the Materials Project.⁴⁴ This bulk structure is cell-optimized to obtain lattice parameters for the BEEF-vdW functional with an 800 eV planewave cutoff and sampled with a (16 × 16 × 8) Monkhorst-Pack *k*-point mesh.⁴⁵ A second cell relaxation using the optimized cell from the first relaxation is performed to minimize the Pulay stress.⁴⁶ A (2 × 2 × 4) surface with 16 Å of vacuum between repeating images in the *z* direction is then constructed from the BEEF-vdW optimized bulk structure. For geometry optimizations, the planewave cutoff is set to 500 eV, and a Monkhorst-Pack *k*-point mesh of (4 × 4 × 1) is used to sample the Brillouin zone. The bottom two layers of the slab are fixed in their bulk positions, while the top two layers of the slab including any adsorbates are allowed to relax. All structures are optimized until forces on all free atoms are less than 0.05 eV/Å. A dipole correction is used to decouple electrostatic interactions between repeating images in the *z* direction.⁴⁷ Images of the optimized slab are presented in Figure 2.

Thermochemical corrections for gas-phase molecules are obtained under the ideal-gas limit, while for adsorbed species all degrees of freedom are treated harmonically to obtain the free energy, $G = E_{\text{electronic}} + \text{ZPE} - TS$. For all thermochemical corrections for gas-phase and adsorbed species in our calculations, please see Table S3 in the SI. To construct the following free energy diagrams (FED), Gibbs free energies for intermediates with adsorbates are referenced to the clean slab, NH₃(g),

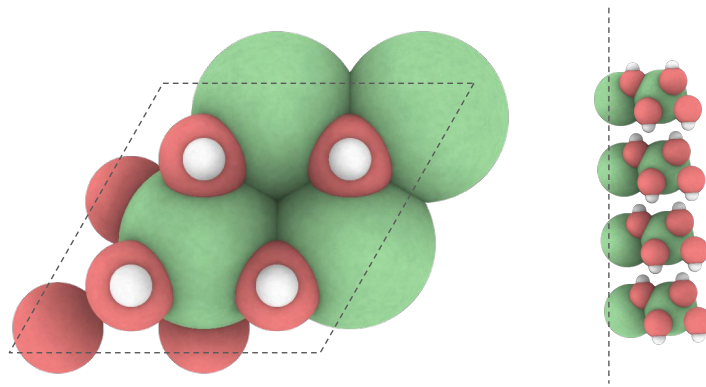


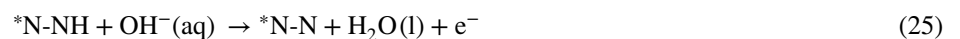
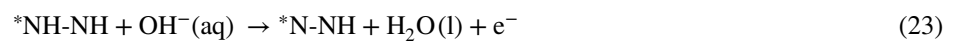
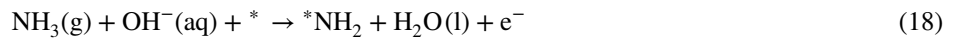
FIGURE 2 Top and side views of β -Ni(OH)₂(001) surface used in this study. A vacuum spacing of 16 Å is present in the *z* direction. White spheres: H; red spheres: O, green spheres: Ni.

H₂(g), and H₂O(l). The free energy of a liquid water molecule is obtained by calculating the free energy of gas phase H₂O at its vapour pressure where the chemical potential of the two phases are equivalent. The free energies of desorption for aqueous nitrite and nitrate are derived from thermodynamic cycles for the dissociation of nitrous and nitric acid, respectively (see the SI for further details). All FEDs use the lowest calculated adsorption free energy for each intermediate which correspond to the most favourable optimized geometry shown below the free energy diagram. Lastly, all Gibbs free energies are shifted to a pH of 11 and the stated applied potential using the computational hydrogen electrode (CHE) developed by Nørskov et al.⁴⁸ and adapted by Chen et al. for basic environments (details are shown in the SI).⁴⁹ This pH value is chosen to reflect experimental conditions in the work of Shih et al.²⁹

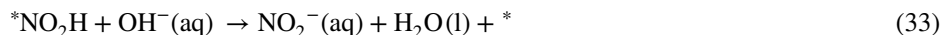
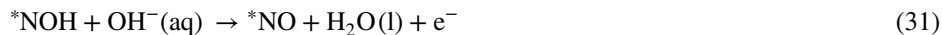
3 | RESULTS AND DISCUSSION

Using the CHE standard protocol, adsorbates are formed with oxygen-containing species originating from the solvent. In other words, a lattice oxygen mechanism is not considered although it is possible that a chemical oxygenation mechanism may also occur, however this is beyond the scope of the present study. Every electrochemical step is considered to proceed via either the removal of a proton-electron pair, or the addition of hydroxide coupled with removal of an electron. For all pathways, the position of adsorbates is tested on all possible sites: atop, three-fold hollow, and bridge, on the (001) facet containing a single OH vacancy (Figure 2). The top and side views of the lowest energy configuration of key intermediates are included in Figures 3–5, indicating that the majority of intermediates favour the three-fold hollow site. The reactions and intermediates considered for all three AOR products in this work are detailed below.

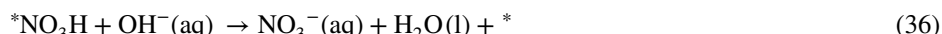
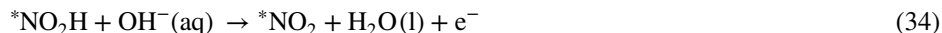
Steps considered in pathway toward dinitrogen formation:



Additional steps considered for nitrite formation:



Additional steps considered for nitrate formation:



3.1 | Dinitrogen formation

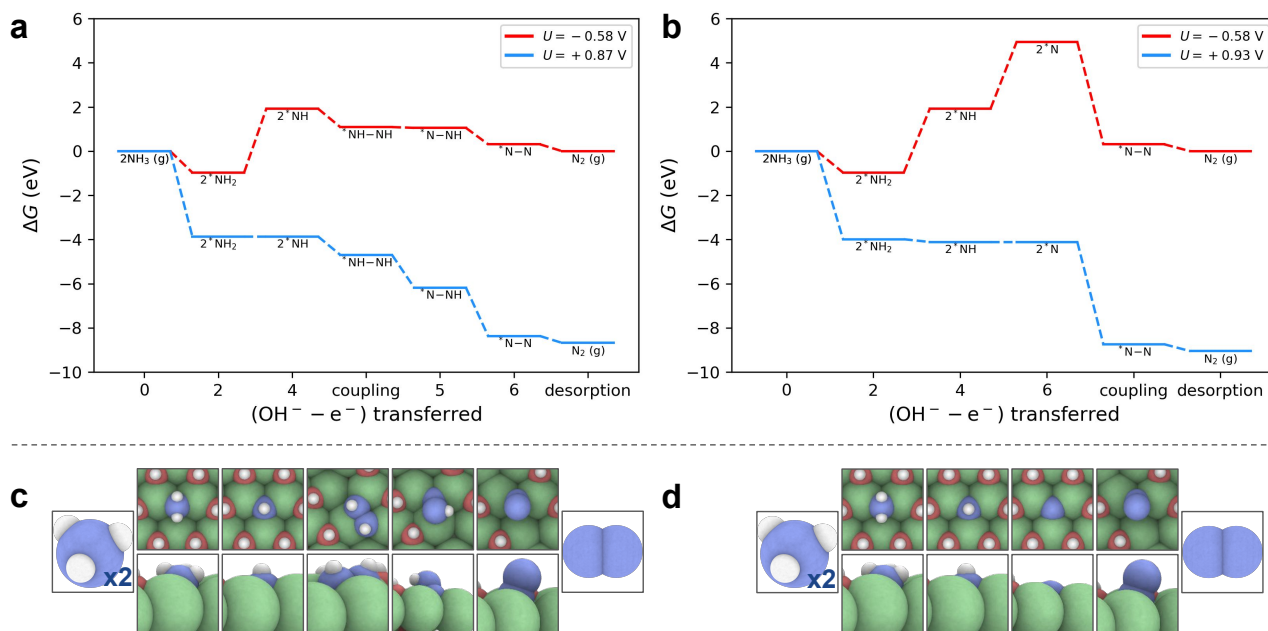


FIGURE 3 Top: Free energy diagrams of $\text{N}_2(\text{g})$ formation from ammonia via (a) $^*\text{NH-NH}$ coupling (Gerischer-Mauerer mechanism)⁷ and (b) $^*\text{N-N}$ coupling (Oswin-Salomon mechanism)⁶ at equilibrium (red trace) and limiting (blue trace) potentials computed using the computational hydrogen electrode at pH 11. Bottom: Top and side views of lowest energy configuration for adsorbates on $\beta\text{-Ni}(\text{OH})_2$ corresponding to (c) Oswin-Salomon path and (d) Gerischer-Mauerer path.

The investigation of the AOR mechanism on $\beta\text{-Ni}(\text{OH})_2$ toward dinitrogen formation begins with the recreation of both the Gerischer-Mauerer mechanism ($\text{NH}_x\text{-NH}_y$ coupling, Figure 3 a) and the Oswin-Salomon mechanism (N-N homocoupling, Figure 3 b). To determine the most likely path, a comparison of free energies for several N-N coupling intermediates was

conducted: $^*\text{NH}_2\text{-NH}_2$, $^*\text{NH-NH}$, $^*\text{N-NH}$, and $^*\text{N-N}$. It was found that while $^*\text{N-N}$ coupling is highly energetically favourable, the formation of $^*\text{N}$ is limiting (Figure 3 b) which is in agreement with DFT works on Pt(111)¹¹ and Pt(100).¹² As the path via $^*\text{N}$ is too uphill, the deprotonation of $^*\text{NH}_2$ to $^*\text{NH}$ becomes the potential determining step. In comparing the value obtained in this work for $\beta\text{-Ni(OH)}_2$ to DFT works on Pt, it seems that the stark difference in the free energy of $^*\text{NH}_2$ deprotonation to $^*\text{NH}$ is a decisive factor in the limiting potential differences between the two materials. For instance, in a work by Katsounaros et al. studying AOR on Pt(100) using DFT,¹² the free energy of this step at pH = 0 and $U = 0$ V is 0.62 eV (converted from $\Delta G_{^*\text{NH}} = 0.57$ eV at 0.057 V_{RHE}) compared to 1.10 eV on $\beta\text{-Ni(OH)}_2$. Thus, this difference in the stabilization of the $^*\text{NH}$ intermediate may explain the more positive onset potential of AOR on $\beta\text{-Ni(OH)}_2$.

Due to the free energy of $^*\text{N}$ formation and the energies of the coupling intermediates studied, $^*\text{NH-NH}$ coupling appears to be the lowest energy path, with a computed limiting potential of 0.87 V_{SHE} at pH 11 (3 a). The formation of dinitrogen via $^*\text{NH-NH}$ coupling is in agreement with theoretical works of AOR on Pt.^{11,12} In particular, the theoretical work of Katsounaros et al. computed that on Pt(100), $^*\text{NH-NH}$ has the lowest combination of free energy of formation and kinetic barrier of all $^*\text{NH}_x\text{-NH}_y$ coupling intermediates.¹² Nevertheless, on $\beta\text{-Ni(OH)}_2$, the computed limiting potential for N_2 formation via $^*\text{N-N}$ homocoupling is 0.93 V_{SHE}, which only represents a small difference of 0.06 V_{SHE} as compared to the onset potential of $^*\text{NH-NH}$ coupling. Lastly, of all coupling intermediates studied, $^*\text{NH}_2\text{-NH}_2$ is the only intermediate that does not form spontaneously during geometry optimization in our study. Katsounaros et al. found that $^*\text{NH}_2\text{-NH}_2$ formation has a high kinetic barrier on Pt(100), which may help explain the same observation on $\beta\text{-Ni(OH)}_2$.¹² It should be noted that the coupling energies presented here only pertain to one level of adsorbate coverage. Recent work by Wallace et al. studying AOR on Pt(100) has demonstrated that the energy of coupling can change with surface coverage, indicating that further investigation may be useful.¹⁵

3.2 | Nitrite and nitrate formation

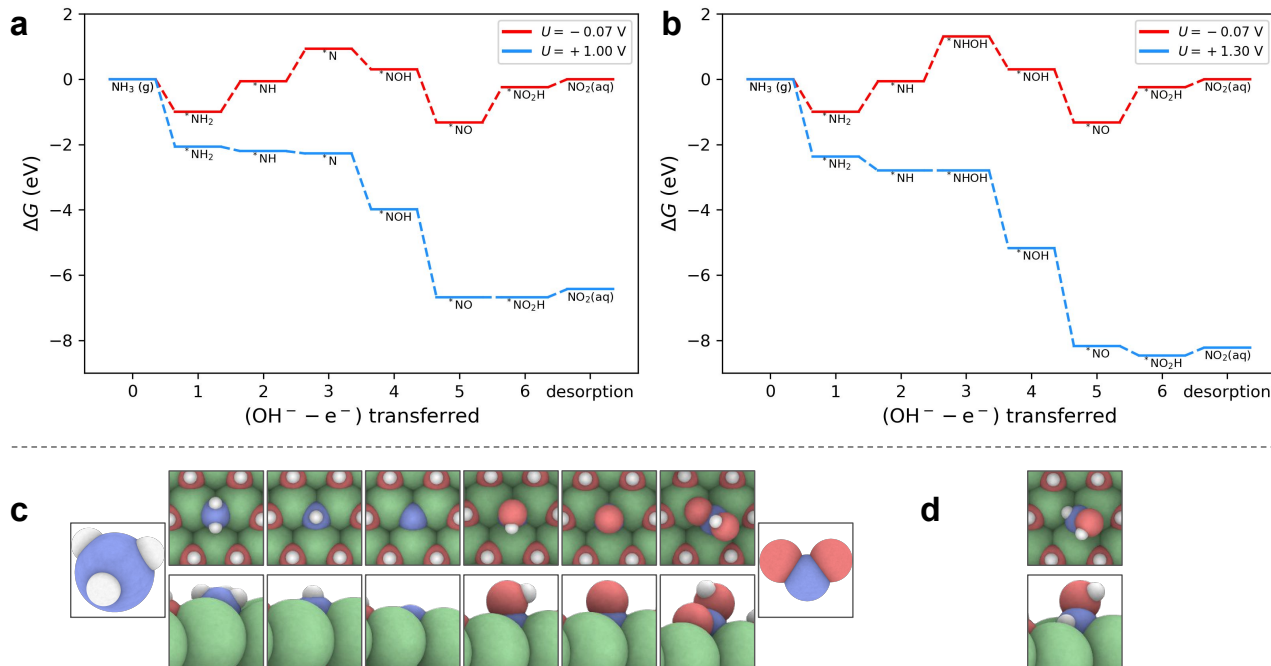
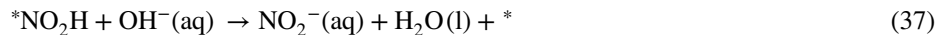
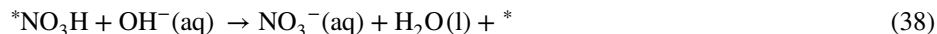


FIGURE 4 Top: Free energy diagrams of $\text{NO}_2^-(\text{aq})$ formation from ammonia via (a) $^*\text{N}$ and (b) $^*\text{NHOH}$ intermediates at equilibrium (red trace) and limiting (blue trace) potentials computed using the computational hydrogen electrode at pH 11. Bottom: Top and side views of (c) lowest energy configurations for AOR intermediates in the path toward $\text{NO}_2^-(\text{aq})$ and (d) $^*\text{NHOH}$, which is the only adsorbate that differs from the previous pathway.

Equations 11 and 17 previously outlined the reduction of nitrite and nitrate based on sequential proton-electron transfers from the solvent, or the transfer of an electron coupled with release of OH^- . The last step in the direction of oxidation for both processes involves a chemical (non-potential dependent) deprotonation coupled with desorption. For nitrite, this is:



And for nitrate, the scheme is:



Using literature thermodynamic data and DFT-based free energies of $^*\text{NO}_2\text{H}$ adsorption, the free energy of nitrite desorption is calculated to be 0.25 eV at pH 11 (see the SI for details). Similarly, the free energy of nitrate desorption is calculated to be 0.1 eV. In an experimental work studying AOR on $\beta\text{-Ni}(\text{OH})_2/\text{NiOOH}$ supported on nickel foam, some nitrite was observed as a product; however, the yield was a tenth of that of nitrate and did not increase with increasing applied potential.²⁹ Nevertheless, given that nitrite yield is variable, special attention must be given to nitrite transformation steps in the context of solvent and pH.

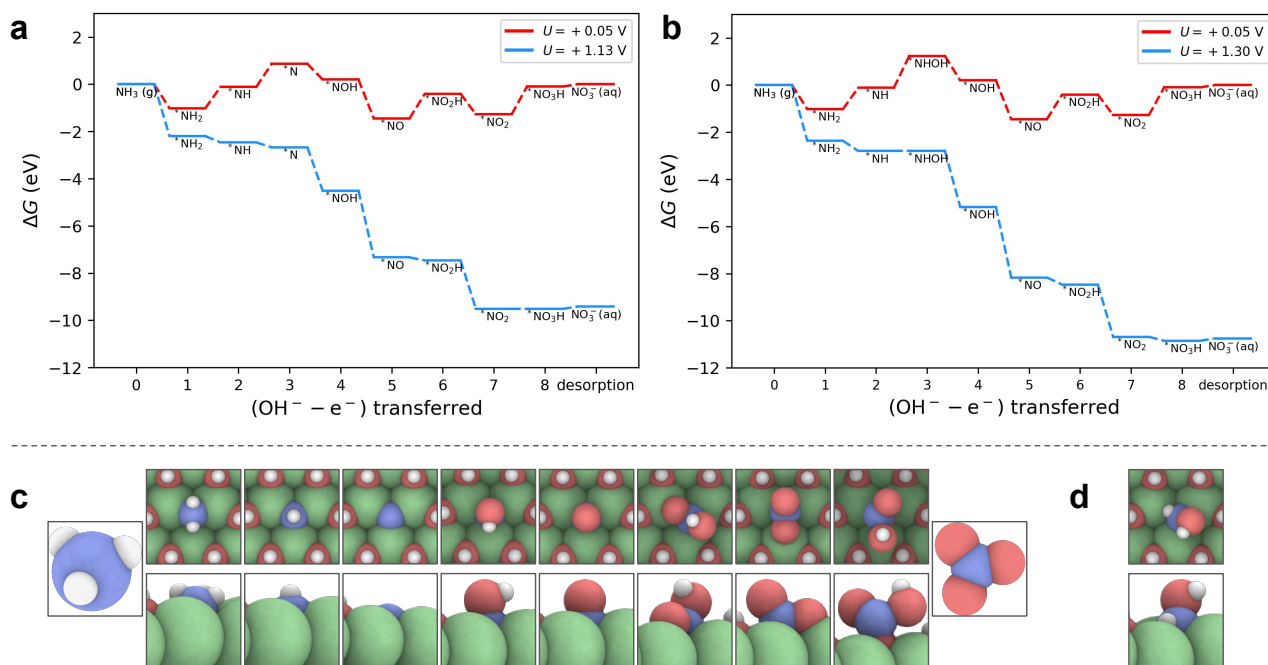


FIGURE 5 Top: Free energy diagrams of $\text{NO}_3^-(\text{aq})$ formation from ammonia via (a) $^*\text{N}$ and (b) $^*\text{NHOH}$ intermediates at equilibrium (red trace) and limiting (blue trace) potentials computed using the computational hydrogen electrode at pH 11. Bottom: Top and side views of (c) lowest energy configurations for AOR intermediates in the path toward $\text{NO}_3^-(\text{aq})$ and (d) $^*\text{NHOH}$, which is the only adsorbate that differs from the previous pathway.

To explore the various pathways toward nitrite and nitrate formation from $\text{NH}_3(\text{g})$, the hydroxylation of all early AOR intermediates, $^*\text{NH}_2$, $^*\text{NH}$, and $^*\text{N}$ to form $^*\text{NH}_2\text{OH}$, $^*\text{NHOH}$, and $^*\text{NOH}$ was considered. Of these possibilities, it was found that the path toward nitrite and nitrate that proceeds via hydroxylation of $^*\text{N}$, that is, via the $^*\text{NOH}$ intermediate, is most energetically favoured (see Figure 4 a) as the formation of $^*\text{NHOH}$ is 0.4 eV higher in energy than $^*\text{N}$. The adsorbate $^*\text{NH}_2\text{OH}$ was found to be unstable and spontaneously forms $^*\text{NH}_2$ and desorbed OH^- .

Once $^*\text{NOH}$ was established as the lowest energy intermediate toward nitrite and nitrate formation, the free energy of $^*\text{NO}$ formation was contrasted with that of $^*\text{NO}_2\text{H}_2$. The free energy of $^*\text{NO}_2\text{H}_2$ is approximately 2.6 eV greater than that of $^*\text{NO}$,

suggesting that the mechanism will go through $^*\text{NO}$ rather than $^*\text{NO}_2\text{H}_2$. $^*\text{NO}$ also appears as an energetic sink in the free energy diagram (Figure 4 a) and will not desorb to form $\text{NO}(\text{g})$ as it is stabilized by 2.2 eV. Given the stability of $^*\text{NO}$ as an intermediate, the oxidation of $^*\text{NO}$ to $^*\text{NO}_2\text{H}$ in the lowest energy path to nitrite is the limiting step, in contrast to the mechanism for dinitrogen formation which is limited by the oxidation of $^*\text{NH}_2$ to $^*\text{NH}$.

The downhill nature of the oxidation of $^*\text{NOH}$ to $^*\text{NO}$ and the stability of the $^*\text{NO}$ adsorbate is another parallel with the DFT literature studying AOR on Pt. On Pt(100), both Katsounaros et al.¹² and Pillai et al.¹³ found that the oxidation of $^*\text{NOH}$ to $^*\text{NO}$ is strongly exothermic. However, on Pt the formation of $^*\text{NOH}$ from the oxidation of $^*\text{N}$ on Pt is quite uphill,¹³ posing a barrier towards further oxidation of surface species. As this transformation occurs spontaneously on $\beta\text{-Ni}(\text{OH})_2$ at both the equilibrium and onset potentials, it appears that reducing the barrier towards $^*\text{N}$ ($\Delta G = 1.58$ eV at pH = 0) and $^*\text{NO}$ ($\Delta G = 1.65$ eV at pH = 0) formation will be the most efficacious in reducing the onset potential of nitrite formation on nickel hydroxide.

The limiting potential for nitrate formation is slightly more positive than that of nitrite (1.13 vs 1.00 V at pH 11) and the limiting step is now the oxidation of $^*\text{NO}_2$ to $^*\text{NO}_3\text{H}$ (Figure 5 a). Similar to $^*\text{NO}$, $^*\text{NO}_2$ is well-stabilized by the hydroxide surface. In a shift from the optimized geometries of previous adsorbates, the nitrogen on $^*\text{NO}_2$ now adsorbs via bridging Ni atoms. This allows one of the oxygen atoms to adsorb to a Ni atom and precipitates a shift from N-oriented adsorption to O-oriented adsorption. Once $^*\text{NO}_2$ is oxidized to $^*\text{NO}_3\text{H}$, the lowest energy adsorbate configuration is no longer adsorption via the N atom. Despite initializing the $^*\text{NO}_3\text{H}$ geometry in a planar configuration with the N atom in the three-fold hollow site, adsorption via O is always the most favoured geometry. Work investigating nitrate reduction on transition metals confirmed that nitrate favours binding via O atoms, although in those cases the favoured geometry is bidentate binding with two oxygen atoms.⁵⁰ To destabilize $^*\text{NO}_2$ to reduce the onset potential of nitrate formation, it may be important to consider the Ni-O binding strength of $\beta\text{-Ni}(\text{OH})_2$ in addition to the Ni-N binding strength.

4 | CONCLUSIONS

The lowest energy pathway towards formation of dinitrogen on the (001) facet of $\beta\text{-Ni}(\text{OH})_2$ was shown to proceed via successive coupled deprotonation-oxidation of NH_3 to $^*\text{NH}$ and subsequent NH-NH coupling, which is in accordance with theoretical works of AOR on Pt(100) and the Gerischer-Mauerer mechanism. The limiting step for the lowest energy pathway was found to be the conversion of $^*\text{NH}_2$ to $^*\text{NH}$. The computed limiting potentials for dinitrogen formation at pH 11 from NH-NH and N-N coupling were 0.87 V and 0.93 V, respectively, while $\text{NH}_2\text{-NH}_2$ coupling did not occur spontaneously.

In the case of nitrite and nitrate formation, the formation of oxygen-containing species proceeds via hydroxylation of $^*\text{N}$. While $^*\text{NHOH}$ formation is theoretically possible, it is ca. 0.4 eV higher in energy than $^*\text{N}$ formation and thus not the favoured intermediate. The formation of nitrite was found to occur via alternating hydroxylation and deprotonation steps (both coupled with a one-electron oxidation), as successive hydroxylation steps led to intermediates with prohibitively high free energies of adsorption. Overall, the DFT-calculated onset potentials for dinitrogen, nitrite, and nitrate formation are in close agreement the experimentally observed onset potentials with the calculated values differing from the experimental values of Shih et al. by 0.03, 0.11, and 0.19 V, respectively. The DFT onset potentials in our study are always slightly more positive than the experimental values, which may suggest that employing charged species or solvation could stabilize key AOR intermediates.

Future work will focus on elucidating the AOR mechanism on the $\beta\text{-NiOOH}$ surface and examining the effect of alloying on the electronic structure of NiO_xH_y materials. Additionally, pathways involving $^*\text{NO}$ coupling should be considered given the apparent stability of this adsorbate and in light of experimental work by Finkelstein et al. on Pt(100) that suggested several possible $^*\text{NH}_x\text{NO}$ intermediates.¹⁶ Lastly, since the reported experimental AOR potentials are in the OER region (Figure 1), future studies should include an analysis of the competition between OER and AOR both with respect to product formation and competition for active sites.

Acknowledgements

RMC and LDC gratefully acknowledge the Natural Sciences and Engineering Research Council of Canada (Discovery Grant) and New Frontiers for Research Fund (Exploration Award) for financial support of this work. All DFT calculations are enabled by Advanced Research Computing resources generously provided by Compute Canada. SWT, RMC and AK thank the University of Waterloo (Startup and Trailblazer Funding), Waterloo Institute for Nanotechnology (WIN-MESA+ Seed Funding), Natural

Sciences and Engineering Research Council of Canada, Canada Foundation for Innovation, and Ontario Research Fund for the financial support.

References

1. N. M. Adli, H. Zhang, S. Mukherjee, G. Wu, *J. Electrochem. Soc.* **2018**, *165*, J3130–J3147
2. R. Abbasi, B. P. Setzler, J. Wang, Y. Zhao, T. Wang, S. Gottesfeld, Y. Yan, *Curr. Opin. Electrochem.* **2020**, *21*, 335–344
3. D. R. MacFarlane, P. V. Cherepanov, J. Choi, B. H. Suryanto, R. Y. Hodgetts, J. M. Bakker, F. M. Ferrero Vallana, A. N. Simonov, *Joule* **2020**, *4*, 1186–1205
4. J. Yao, Y. Mei, G. Xia, Y. Lu, D. Xu, N. Sun, J. Wang, J. Chen, *Int. J. Environ. Res. Public Health* **2019**, *16*, year
5. X. V. Medvedeva, J. J. Medvedev, S. W. Tatarchuk, R. M. Choueiri, A. Klinkova, *Green Chem.* **2020**, *22*, 4456–4462
6. H. G. Oswin, M. Salomon, *Can. J. Chem.* **1963**, *41*, 1686–1694
7. H. Gerischer, A. Mauzer, *J. Electroanal. Chem.* **1970**, *25*, 421–433
8. G. Novell-Leruth, A. Valcárcel, A. Clotet, J. M. Ricart, J. Pérez-Ramírez, *J. Phys. Chem. B* **2005**, *109*, 18061–18069
9. V. Rosca, M. T. Koper, *Phys. Chem. Chem. Phys.* **2006**, *8*, 2513–2524
10. G. Novell-Leruth, J. M. Ricart, J. Pérez-Ramírez, *J. Phys. Chem. C* **2008**, *112*, 13554–13562
11. J. A. Herron, P. Ferrin, M. Mavrikakis, *J. Phys. Chem. C* **2015**, *119*, 14692–14701
12. I. Katsounaros, M. C. Figueiredo, F. Calle-Vallejo, H. Li, A. A. Gewirth, N. M. Markovic, M. T. Koper, *J. Catal.* **2018**, *359*, 82–91
13. H. S. Pillai, H. Xin, *Ind. Eng. Chem. Res.* **2019**
14. A. O. Elnabawy, J. A. Herron, S. Karraker, M. Mavrikakis, *J. Catal.* **2021**, *397*, 137–147
15. S. W. Wallace, I. T. McCrum, M. J. Janik, *Catal. Today* **2021**, *371*, 50–57
16. D. A. Finkelstein, E. Bertin, S. Garbarino, D. Guay, *J. Phys. Chem. C* **2015**, *119*, 9860–9878
17. L. Song, Z. Liang, Z. Ma, Y. Zhang, J. Chen, R. R. Adzic, J. X. Wang, *J. Electrochem. Soc.* **2018**, *165*, J3095–J3100
18. K. Siddharth, Y. Chan, L. Wang, M. Shao, *Curr. Opin. Electrochem.* **2018**, *9*, 151–157
19. A. de Voos, M. Koper, R. van Santen, J. van Veen, *J. Electroanal. Chem.* **2001**, *506*, 127–137
20. F. Vidal-Iglesias, N. Garcia-Araez, V. Montiel, J. Feliu, A. Aldaz, *Electrochem. commun.* **2003**, *5*, 22–26
21. S. Wasmus, E. Vasini, M. Krausa, H. Mishima, W. Vielstich, *Electrochim. Acta* **1994**, *39*, 23–31
22. N. J. Bunce, D. Bejan, *Electrochim. Acta* **2011**, *56*, 8085–8093
23. D. J. G. Speight, *Lange's Handbook of Chemistry, Seventeenth Edition*, McGraw-Hill Education, New York, 17th ed., **2017**
24. M. Görlin, J. Halldin Stenlid, S. Koroidov, H.-Y. Wang, M. Börner, M. Shipilin, A. Kalinko, V. Murzin, O. V. Safonova, M. Nachttegaal, A. Uheida, J. Dutta, M. Bauer, A. Nilsson, O. Diaz-Morales, *Nat. Commun.* **2020**, *11*, 6181
25. L. Zhang, L. Wang, H. Lin, Y. Liu, J. Ye, Y. Wen, A. Chen, L. Wang, F. Ni, Z. Zhou, S. Sun, Y. Li, B. Zhang, H. Peng, *Angew. Chemie - Int. Ed.* **2019**, *58*, 16820–16825
26. S. W. Tatarchuk, R. M. Choueiri, X. V. Medvedeva, L. D. Chen, A. Klinkova, *Chemosphere* **2021**, *279*, 130550

27. A. Kapalka, A. Cally, S. Neodo, C. Comninellis, M. Wächter, K. M. Udert, *Electrochem. commun.* **2010**, *12*, 18–21
28. W. Xu, R. Lan, D. Du, J. Humphreys, M. Walker, Z. Wu, H. Wang, S. Tao, *Appl. Catal. B Environ.* **2017**, *218*, 470–479
29. Y.-J. Shih, Y.-H. Huang, C. Huang, *Electrochim. Acta* **2018**, *263*, 261–271
30. X. Jiang, D. Ying, X. Liu, M. Liu, S. Zhou, C. Guo, G. Zhao, Y. Wang, J. Jia, *Electrochim. Acta* **2020**, *345*, 136157
31. D. S. Hall, D. J. Lockwood, C. Bock, B. R. MacDougall, *Proc. R. Soc. A Math. Phys. Eng. Sci.* **2015**, *471*, 20140792
32. G. Kresse, J. Hafner, *Phys. Rev. B* **1993**, *47*, 558–561
33. G. Kresse, J. Furthmüller, *Comput. Mater. Sci.* **1996**, *6*, 15–50
34. G. Kresse, J. Furthmüller, *Phys. Rev. B* **1996**, *54*, 11169–11186
35. A. Hjorth Larsen, J. Jørgen Mortensen, J. Blomqvist, I. E. Castelli, R. Christensen, M. Dułak, J. Friis, M. N. Groves, B. Hammer, C. Hargus, E. D. Hermes, P. C. Jennings, P. Bjerre Jensen, J. Kermode, J. R. Kitchin, E. Leonhard Kolsbjerg, J. Kubal, K. Kaasbjerg, S. Lysgaard, J. Bergmann Maronsson, T. Maxson, T. Olsen, L. Pastewka, A. Peterson, C. Rostgaard, J. Schiøtz, O. Schütt, M. Strange, K. S. Thygesen, T. Vegge, L. Vilhelmsen, M. Walter, Z. Zeng, K. W. Jacobsen, *J. Phys. Condens. Matter* **2017**, *29*, 273002
36. J. Wellendorff, K. T. Lundgaard, A. Møgelhøj, V. Petzold, D. D. Landis, J. K. Nørskov, T. Bligaard, K. W. Jacobsen, *Phys. Rev. B* **2012**, *85*, 235149
37. P. E. Blöchl, *Phys. Rev. B* **1994**, *50*, 17953–17979
38. G. Kresse, D. Joubert, *Phys. Rev. B* **1999**, *59*, 1758–1775
39. A. Szytula, A. Murasik, M. Balanda, *Phys. Status Solidi* **1971**, *43*, 125–128
40. Z. Szotek, W. M. Temmerman, H. Winter, *Phys. Rev. B* **1993**, *47*, 4029–4032
41. J. A. Majewski, P. Vogl, *Phys. Rev. B* **1992**, *46*, 12219–12234
42. P. Hermet, L. Gourrier, J. L. Bantignies, D. Ravot, T. Michel, S. Deabate, P. Boulet, F. Henn, *Phys. Rev. B - Condens. Matter Mater. Phys.* **2011**, *84*, 1–10
43. V. Kazimirov, M. Smirnov, L. Bourgeois, L. Guerlou-Demourgues, L. Servant, A. Balagurov, I. Natkaniec, N. Khasanova, E. Antipov, *Solid State Ionics* **2010**, *181*, 1764–1770
44. A. Jain, S. P. Ong, G. Hautier, W. Chen, W. D. Richards, S. Dacek, S. Cholia, D. Gunter, D. Skinner, G. Ceder, K. A. Persson, *APL Mater.* **2013**, *1*, 011002
45. H. J. Monkhorst, J. D. Pack, *Phys. Rev. B* **1976**, *13*, 5188–5192
46. G. P. Francis, M. C. Payne, *J. Phys. Condens. Matter* **1990**, *2*, 4395–4404
47. L. Bengtsson, *Phys. Rev. B* **1999**, *59*, 12301–12304
48. J. K. Nørskov, J. Rossmeisl, A. Logadottir, L. Lindqvist, J. R. Kitchin, T. Bligaard, H. Jónsson, *J. Phys. Chem. B* **2004**, *108*, 17886–17892
49. L. D. Chen, J. K. Nørskov, A. C. Luntz, *J. Phys. Chem. Lett.* **2015**, *6*, 175–179
50. J.-X. Liu, D. Richards, N. Singh, B. R. Goldsmith, *ACS Catal.* **2019**, *9*, 7052–7064

How to cite this article: R. M. Choueiri, S. W. Tatarchuk, A. Klinkova, and L. D. Chen (2021), Mechanism of Ammonia Oxidation to Dinitrogen, Nitrite, and Nitrate on β -Ni(OH)₂ from First-Principles Simulations, *Electrochem. Sci. Adv.*, 2021;XX:X–X.